

Simulation and Property Characterization of Nanoparticle Thermal Conductivity for a Microscale Selective Laser Sintering System

Joshua Grose¹, Obehi G. Dibua¹, Dipankar Behera¹, Chee S. Foong², Michael Cullinan^{1*}

¹ The University of Texas at Austin, Department of Mechanical Engineering, Austin, TX

² NXP Semiconductor inc., Austin, TX

ABSTRACT

Current Additive Manufacturing (AM) technologies are typically limited by the minimum feature sizes of the parts they can produce. This issue is addressed by the microscale selective laser sintering system (μ -SLS), which is capable of building parts with single micrometer resolutions. Despite the resolution of the system, the minimum feature sizes producible using the μ -SLS tool are limited by unwanted heat dissipation through the particle bed during the sintering process. To address this unwanted heat flow, a particle scale thermal model is needed to characterize the thermal conductivity of the nanoparticle bed during sintering and facilitate the prediction of heat affected zones (HAZ). This would allow for the optimization of process parameters and a reduction in error for the final part. This paper presents a method for the determination of the effective thermal conductivity of copper nanoparticle beds in a μ -SLS system using finite element simulations performed in ANSYS. A Phase Field Model (PFM) is used to track the geometric evolution of the particle groups within the particle bed during sintering. CAD models are extracted from the PFM output data at various timesteps, and steady state thermal simulations are performed on each particle group. The full simulation developed in this work is scalable to particle groups with variable sizes and geometric arrangements. The particle thermal model results from this work are used to calculate the thermal conductivity of the copper nanoparticles as a function of the density of the particle group.

INTRODUCTION

*michael.cullinan@austin.utexas.edu

29 Commercially available Additive Manufacturing (AM) systems are typically
30 capable of producing parts with feature sizes on the order of hundreds of micrometers
31 [1,2]. Although these manufacturing processes are versatile, this size limitation prevents
32 their effective use in the microelectronics industry, where parts require manufacturing
33 resolutions on the order of a few micrometers. The leading process used to manufacture
34 two and a half dimensional microelectronics structure consists of a mixture of
35 lithography, etching and chemical deposition steps, which often require intricate setups
36 and suffer from size limitations. The development of a microscale selective laser sintering
37 (μ -SLS) system addresses the need for a more robust, flexible, and easy to use process,
38 while targeting a minimum feature size on the order of a single micrometer [3-6].

39 Selective Laser Sintering (SLS) is an AM process that directly applies laser energy
40 to a deposited powder bed. The laser energy increases the temperature within the bed in
41 the areas of laser application which facilitates the fusion of the powder particles into a
42 solid part. This sintering process is repeated for each subsequently deposited layer until
43 a full part is formed [7]. One of the major advantages of SLS over other commercial AM
44 systems is its ability to build true 3D parts, such as overhanging structures, due to support
45 provided by the unsintered material adjacent to the sintered part. The μ -SLS system
46 functions similarly to traditional SLS processes in that laser irradiation is applied to a
47 particle bed and the process is repeated layer-by-layer. The primary difference between
48 the two processes is the use of nanoparticles as the powdered material in the μ -SLS
49 system, which facilitates the production of parts with single micrometer features. Given

50 the scale of these particles and the required feature sizes, accurate characterization of
51 the nanoparticle beds is needed to optimize the μ -SLS process.

52 Existing simulation work for SLS systems provide insight into the general process
53 of heat transfer in powdered systems [8-10], although they focus on larger particles and
54 typically model a melting and solidification process, as opposed to the solid-state
55 sintering process experienced by the nanoparticles used in the μ -SLS system. These
56 particles are on the order of 10-100 nanometers in diameter. The nanoparticles remain
57 solid as they sinter, with grain boundary and surface diffusion dominating the underlying
58 solid-state sintering mechanisms [11]. The effective thermal conductivity of metal
59 nanoparticles within a powder bed system is found to be dominated by the evolving
60 geometries of the nanoparticles as they diffuse into one another, and the grain boundary
61 thermal contact resistance at the interfaces between adjacent nanoparticles [12]. The
62 work presented in this paper focuses on these two dominating factors, while also
63 considering the conductivities of the individual copper nanoparticles and the surrounding
64 air medium.

65

66 **BACKGROUND**

67 The modeling and simulation of the heat transfer characteristics and material
68 properties of particle systems has been actively researched for years. Two-particle models
69 have been developed to predict heat transfer between adjacent particles in thermal
70 contact using analytical and computational methods. The two-particle model developed
71 by Bachelor and O'Brien [13] was used to determine the effective conductivity of a

72 granular material experiencing steady state heat transfer conditions. The model assumes
73 heterogeneous media which allows it to capture the stochastic nature of particle
74 packings. Sun and Chen [14] developed a particle conduction model that uses Hertzian
75 contact theory to estimate the contact area between two adjacent particles. The model
76 makes a critical assumption that the bodies in contact behave as semi-infinite solids,
77 where changes in temperature due to the contacts between particles are confined to a
78 small region surrounding the contact area. Although it reduces the computational
79 complexity of the model, the semi-infinite solid approximation reduces the accuracy of
80 Sun and Chen's model for larger Fourier numbers. Zhou, Yu and Horio [15] worked to
81 improve the work by Sun and Chen by developing a finite element simulation of a particle-
82 particle collision system to provide a correction factor for large Fourier numbers.
83 Similarly, Shimizu [16] developed a particle conduction model where heat is transferred
84 between adjacent particles through a thermal pipe with a cross sectional area equal to
85 the expected contact area between the two particles. Two particle conduction models
86 like those developed by Bachelor and O'Brien, Sung and Chen and Shimizu can be
87 expanded to particle systems with more than 2 particles given the assumed independence
88 of particle-particle contacts. However, this typically requires extensive computational
89 resources, and fails to account for time-varying, non-spherical geometries and the use of
90 nanoparticles in the models.

91

92 Models capable of estimating the effective material properties and heat transfer
93 characteristics of aerogels consisting of packed nanoparticles have recently been

94 developed. Zhao et al. [17] developed a diffusion-limited colloidal aggregation model to
95 determine particle packing structures in silica aerogels and determine the effective
96 thermal conductivity of the structure using a 3D finite volume numerical model. This work
97 considers the effects of the random particle packing structures, the solid-gas coupling,
98 conduction within solid particles, and the area of contact between adjacent particles to
99 calculate the conductivity values. Guo and Tang [18] built a theoretical model that focused
100 on the relative effects of particle-particle conduction in the solid particle chains, particle-
101 air-particle conduction along the particle chains, and heat conduction from the particle
102 chains to the surrounding pore gas. Although these conductivity models provide insight
103 on relevant heat transfer parameters in nanoparticle systems, they analyze insulative
104 materials and packing structures unlike those found in μ -SLS systems. They also do not
105 consider the geometric evolution of the nanoparticles that occurs during a temperature
106 driven solid state diffusion process.

107

108 Work has also been developed that considers the varying sizes and packing
109 structures of nanoparticles of various materials. These research efforts determine the
110 relationship between the porosity of the nanoparticle structure and its effective thermal
111 conductivity. Wu and Huang [19] prepared SiC nanoparticle beds and measured the
112 thermal conductivity of the system. They also developed a thermal model that accounted
113 for thermal contact resistance between particles and the thermal contact resistance
114 between nanoparticles and the surrounding air. Using this model and corresponding
115 experimental data, Wu and Huang developed a relationship between the particle packing

116 density (represented as porosity) and the effective thermal conductivity of the SiC
117 nanoparticles to quantify SiC capabilities as an insulator. Lin et al. [20] used the transient
118 hot-wire method to measure the thermal conductivity changes of copper and nickel
119 nanoparticle packed beds as a function of the changing porosity during sintering at
120 various temperature. They also analyzed the effects of the tableting pressure in
121 enhancing the conductivity of these structures. Qin et al. [21] also investigated the
122 relationship between porosity and thermal conductivity for groups of metal
123 nanoparticles. Specifically, they investigated the effective thermal conductivity for silver
124 nanoparticles undergoing sintering using multiple analytical methods that factored in the
125 relative conductivities of silver and the surrounding pore media. Although these research
126 efforts developed relationships between particle packing porosity and effective thermal
127 conductivity, they focus on porosity values that are much smaller than those experienced
128 by the nanoparticles in the μ -SLS process. These porosity-thermal conductivity
129 relationships also lack a full representation of the geometric evolution of particle
130 geometries during the early sintering and neck formation stage, where porosities are high
131 and effective thermal conductivities continue to be dominated by particle-particle
132 contact resistances.

133

134 Expanding upon more general conduction models, particle heat transfer
135 simulations for SLS systems have been developed for error minimization and part
136 prediction. Ganeriwala and Zohdi [22] developed a coupled finite difference – discrete
137 element method (DEM) model to predict thermal behavior SLS systems. Particles were

138 assumed to be discrete spheres of various sizes, and the substrate was discretized for a
139 finite difference solution. The model analyzes a subsection of a larger particle bed and
140 provides information from the particle scale model to a larger continuum part scale
141 model. Similarly, Moser et al. developed a DEM model to estimate the effective thermal
142 conductivity of particle packings in an SLS powder bed [23,24]. Moser's model assumes
143 all particles in the system are uniform temperature bodies. The primary heat transfer
144 modes considered by this model are particle-particle conduction, particle-gas-particle
145 conduction and radiation when determining the steady state temperature distribution in
146 the particle system. The output temperature values were used to calculate the effective
147 thermal conductivity of the randomly generated group of particles. Although these SLS
148 models effectively simulating the heat transfer process within powder beads for the initial
149 spherical arrangement of particles, they model a particle melting and solidification
150 process. In the μ -SLS system, sintering is a solid-state diffusion process, where the
151 particles do not undergo phase transformations. Therefore, as the particles diffuse into
152 each other, the resulting geometries of the particle groups change significantly despite
153 the lack of a phase change. This work builds upon previous research efforts and expands
154 their scope to incorporate the complex geometric changes experienced by the
155 nanoparticle powders undergoing laser sintering and estimates the effective thermal
156 conductivity of these particle packings as a function of sintering duration.

157

158 **MODELING METHODS**

159 A Finite Element Model (FEM) was developed in this work to determine the
160 effective thermal conductivity of copper nanoparticles as a function of densification in a
161 μ -SLS system. A steady state heat transfer simulation was performed in ANSYS Mechanical
162 to obtain temperature information within a heated nanoparticle packing. The Finite
163 Element method was selected due to its proven accuracy, setup simplicity and its
164 widespread use in Additive Manufacturing (AM) applications [25,26]. Nanoparticle
165 packings, composed of approximately 20-30 nanoparticles (each on the order of 10-100
166 nanometers in diameter), are analyzed as they transition from discrete spherical particles
167 to a coalesced, sintered unit [27]. Computer aided design (CAD) models are used to
168 represent the packed nanoparticle geometries during the finite element analysis. Surface
169 and grain boundary diffusion is simulated using a Phase Field Model (PFM) to track the
170 morphological evolution of the particles and obtain accurate solid models of the
171 nanoparticles throughout the sintering process [28]. The PFM tracks the evolution of a
172 fixed number of equally spaced points within a defined bounding box. The initial number
173 of particles, the radii of each particle, and the dimensions of the bounding box are variable
174 inputs to the model. For a given particle set, the PFM simulates the entire sintering
175 process and records snapshots of the phase field variables at several timesteps. The
176 captured snapshots provide data files containing a set of phase field variables for each
177 point within the model's bounding box. The data files provide information regarding the
178 particle density, ρ , of the region corresponding to the point in space, as well as a number
179 of η variables equal to the total number of initial particles in the system. Each η variable
180 provides information regarding the contribution each point in the PFM makes to the

181 corresponding particle in the system. Both variables range from 0 to 1 and have cutoffs
182 that determine the geometric arrangement of the nanoparticles. The ρ cutoff determines
183 the threshold between the solid and vapor phases (0 representing vapor, and 1
184 representing solid), and the η variable cutoff determines which points within the
185 bounding box correspond to which particles in the system (0 representing no
186 contribution, and 1 representing full contribution to a specific particle). This dataset is the
187 basis for the subsequent conversion and FEM processes discussed in this paper.

188 **Conversion from PFM Data to CAD Models**

189 Although the PFM data files provide a comprehensive description of the particle
190 geometries throughout the sintering process, the raw data is not a usable geometric input
191 for a finite element solver. FEMs accept solid models and surface bodies in several forms.
192 To use the PFM data in a Finite Element simulation, a conversion process must be
193 established to transform the PFM output data files into usable solid models for FEM input.
194 To accomplish this, a 3-step conversion process is developed. To maintain the accuracy of
195 the PFM output data, this conversion process must provide input CAD files that match the
196 original PFM particle detail. The conversion process must also work for all possible initial
197 particle arrangements, variable particle numbers, and the different geometries that occur
198 as particles diffuse into one another. The steps of the conversion process are as follows.

199 The first step of the conversion process converts raw PFM data into cartesian point
200 clouds. The PFM output data is filtered using the ρ cutoff to determine the solid phase,
201 and the η variable cutoffs are used to divide the domain into individual particles. The

202 resulting collection of filtered points is then run through a surface extraction algorithm to
203 isolate the exterior points and convert the data into a point cloud format. The algorithm
204 evaluates each solid point to see if any of the surrounding points are in the vapor phase
205 and writes a new data file with the filtered surface set. An example of a resulting point
206 cloud is shown in Fig 1a.

207 The second conversion step takes the point cloud coordinate files as input and
208 outputs reconstructed surface meshes for each nanoparticle. These surface meshes are
209 hollow shells composed of small surface triangles and are constructed based on the
210 arrangement of points in the input point cloud. This step in the conversion process is
211 performed in Meshlab, an open-source 3D meshing and reconstruction software, where
212 parameters are adjusted to optimize a tradeoff between surface mesh accuracy and the
213 number and quality of the resulting triangle surface meshes. The major sub steps
214 performed in Meshlab include computation of surface normals, surface reconstruction,
215 surface decimation (a reduction in the number of node points that make up the triangular
216 surface mesh), mesh repair and mesh smoothing. This surface meshing step is often the
217 most critical, as it determines the usability, complexity and surface quality of the
218 downstream solid parts and subsequent finite element meshes. An example of the
219 resulting surface mesh is shown in Fig 1b.

220 The third step of the conversion process takes triangular surface meshes as input,
221 and outputs solid CAD models with defined grain boundaries between adjacent particles.
222 Particle surface meshes are first filled out to form solid CAD models in FreeCAD, an open-

223 source CAD software. The particle models are then checked for holes that result from
224 initial flaws in the surface mesh reconstruction process. Once the particle models are free
225 of defects, a Python script is executed to detect intersections between adjacent
226 nanoparticles in the particle set. This script checks to see if any two particles have
227 overlapping points in their original cartesian point cloud. The information for each pair of
228 overlapping particles is added to an intersection matrix for further processing. The
229 intersection matrix controls a separate Python script with FreeCAD integration that
230 performs particle-particle Boolean cuts. If a small and large particle overlap, the overlap
231 region is removed from the smaller particle to simulate the process of smaller particles
232 diffusing into larger particles. This occurs for each set of intersecting particles recorded in
233 the intersection matrix. These Boolean cuts ensure that the grain boundaries between
234 adjacent nanoparticles in the particle set are correctly modeled, and that the interface
235 between any set of two particles in contact is a perfect fit. This step is critical, as the
236 thermal contact resistance between adjacent nanoparticles in a particle set is one of the
237 most important input parameters in subsequent finite element simulations. This step
238 concludes with two additional operations using FreeCAD Python commands. First, a
239 rectangular block of air with dimensions equal to the PFM bounding box is inserted into
240 the modeling space. This block represents the air surrounding the nanoparticles and is
241 included to allow the FEM to correctly model particle-air-particle conduction. This model
242 neglects natural convection effects due to the extremely small Raleigh numbers, and
243 correspondingly small heat transfer coefficients present in this nanoscale system. In the
244 absence of external forced convection, the surrounding air can be modeled as a solid,

245 thermally conductive medium that remains stationary for the duration of the simulation.
246 To ensure perfect contact between the solid air block and the nanoparticle CAD models,
247 another Python script is used to subtract each particle in the set from the surrounding air
248 block. This forms a hollowed-out block that perfectly envelops the nanoparticle packing.
249 Finally, a second block is inserted beneath the nanoparticles to model the glass substrate.
250 Examples of the completed CAD models are shown in Fig 1.

251 **Conversion from PFM Data to CAD Models**

252 The purpose of converting the PFM output data files to solid CAD models is to
253 prepare the nanoparticle models for FEM. With proper setup, the FEM will solve for a 3D
254 temperature distribution within the nanoparticle models and the surrounding air block,
255 which will be subsequently used to extract the effective thermal conductivity of the
256 particle set. The FEM solver used in this work is configured to solve the heat conduction
257 equation

$$258 \quad \rho c_p \frac{\partial T}{\partial t} = \nabla \cdot (k \nabla T) + Q''' \quad (1)$$

259 where k , ρ , c_p , and Q''' represent the thermal conductivity, the density, the specific heat
260 capacity at constant pressure, and the internal volumetric heat generation of a given solid
261 object. The terms on the right-hand side of Eq. 1 describe the second order spatial
262 temperature gradient in the object summed with the heat generation occurring within
263 that object, Q''' . The term on the left-hand side of Eq. 1 represents the transient thermal
264 response of the object given its material properties. To solve this second-order partial

265 differential equation for the spatial temperature distribution within an object, the
266 nanoparticle CAD models must first be transferred to the finite element workspace,
267 where the finite element meshing algorithm will divide each of the bodies into discrete
268 elements and nodes on which an approximate solution can be solved. Then, heat transfer
269 boundary conditions must be specified. Finally, values for the thermal contact
270 conductance between adjacent nanoparticles and at particle-air interfaces are
271 determined and set. Mesh discretization, boundary condition application and thermal
272 contact conductance determination were the key focuses of the finite element setup.

273 *Mesh Generation*

274 Once the nanoparticle models, the enveloping air block and the glass substrate
275 are brought into the finite element workspace, a multistep meshing procedure is
276 implemented. Due to the nature of the conversion process, the resulting particle models
277 have surface profiles that match their corresponding triangular surface meshes. These
278 profiles are composed of many small triangular faces of varying sizes, adding complexity
279 to the geometry of each nanoparticle. The surrounding air block envelops these particles
280 with matching faces at the contact points, and thus has a similar level of geometric
281 complexity. To account for this, heavily refined meshes are generated both within solid
282 volumes and on planar surfaces. The surface and body meshes are generated separately
283 with unique values to ensure an optimal mesh. Within the particle models and the
284 surrounding air block, a fine tetrahedral mesh is applied. This mesh is restricted to a
285 region of influence near the contact surfaces between the particle models and the solid

286 air block. Hollow spheres of influence are generated and imported into the model to
287 accomplish this volumetric meshing procedure. Each of the hollow spheres of influence
288 encompasses the surface of one of the nanoparticles in the particle set. Both the air and
289 particle models are meshed with this method, allowing for a fine mesh near contact
290 regions, and a coarser mesh near the particle centers. This reduces mesh complexity and
291 reduces overall computational time while emphasizing the regions with fine geometric
292 detail. Additionally, a fine surface mesh is applied to all particle- air contact surfaces. This
293 allows the meshing algorithm to handle the large number of small triangular faces present
294 in the model. Finally, the global mesh is instructed to automatically refine the mesh
295 further in tight spaces to improve the success rate of the meshing algorithm and facilitate
296 subsequent Finite Element modeling.

297 *Boundary Condition Application*

298 After the mesh settings are finalized for all surfaces and solid bodies, boundary
299 conditions representing heat transfer processes are applied to the particle model. Prior
300 to importing the solid models into ANSYS, the edges of the nanoparticle group are
301 removed by a vertical cutting plane to allow for the consistent application of boundary
302 conditions to smooth, vertical faces irrespective of initial conditions or timesteps. The
303 locations of the vertical cuts are chosen such that the fraction of the resulting flat surface
304 area that contains particle faces approximates the volume fraction of the nanoparticles
305 with respect to the bounding box. This boundary modification helps maintain a uniform
306 heat flow across different particle geometries. A coordinate direction is chosen, and a

307 constant temperature of 22 °C is applied to the flat particle faces corresponding the
308 minimum value of this coordinate direction. A constant heat flux of $10^4 \frac{MW}{m^2}$ is then applied
309 to the flat particle faces corresponding to the maximum value of the chosen coordinate
310 direction. All remaining boundary faces in the model are insulated to simulate 1-
311 dimensional heat flow through the nanoparticle set. Radiation was neglected in the
312 model, as it has been found to be negligible compared to particle-particle conduction and
313 particle-air-particle conduction. This is largely due to the relatively low average sintering
314 temperature of roughly 700 K [29]. Applied boundary conditions are depicted in Fig 2c
315 and Fig 2d.

316 *Thermal Contact Conductance*

317 The thermal contact conductance values used in the simulation determine the
318 temperature jumps at the interfaces between adjacent bodies in particle-particle contact
319 and in particle- air contact. The thermal contact conductance for particle-air contact is set
320 to $10^5 \frac{MW}{m^2K}$ to accurately model perfect wetting of the particle surfaces by the surrounding
321 air. The resulting temperature jump at these interfaces should be close to zero to
322 approximate ideal contact between an object and a surrounding fluid. The thermal
323 contact conductance for particle-particle contact is more difficult to estimate. Multiple
324 thermal contacts occur from one end of the nanoparticle packing to the other along the
325 specified coordinate axis. This is especially true for earlier timesteps, where more particle-
326 particle contacts exist along the primary axis of heat flow. A value of $20 \frac{MW}{m^2K}$ was chosen
327 for the particle-particle thermal contact conductance based on estimations from [29] and

328 [30]. The former used DEM to compare relevant heat flows between spherical metal
329 nanoparticles and selected the value of thermal contact conductance that corresponded
330 to the transition point at which the temperature gradients within individual particles
331 became negligible compared to the temperature drop across particle-particle contacts.
332 The latter measured the thermal contact conductance between deposited metal films (Al,
333 Ag, Sn, Zn, and In) and an underlying copper film using transient thermo-reflectance
334 methods. The values determined from [30] ranged from 8 to $95 \frac{MW}{m^2K}$ for the set of tested
335 metals. The value obtained from [29], $20 \frac{MW}{m^2K}$ was determined for the same nanoparticle
336 sintering system as covered in this work. Therefore, the value from [29] was used in this
337 paper for consistency.

338 **RESULTS AND DISCUSSION**

339 The densification of 10 one-by-one micrometer beds consisting of anywhere
340 between 21 and 43 particles was simulated using the PFM setup described earlier. The
341 simulation boxes containing the particle sets were 104 by 104 pixels in the x-y plane and
342 ranged from 56 to 86 pixels along the z-axis. PFM output data files representing
343 nanoparticle geometries for each of the 10 sintered beds were saved at 35 timesteps
344 along the sintering timeline. Each output file was converted into a set of particle CAD
345 models with well-defined contact regions. Each of these particle sets was then imported
346 into an ANSYS Mechanical FEM workspace where mesh generation and boundary
347 condition application were performed before ultimately solving each model for the
348 resulting steady-state temperature distribution within the nanoparticle system.

349 Upon completion of the FEM simulation for each timestep, the temperature distributions
350 were analyzed to calculate the effective conductivity of the particle set. To calculate the
351 effective thermal conductivity of a particle set, the steady state, 1-dimensional
352 approximation to Fourier's law of heat conduction was rearranged and solved for the
353 thermal conductivity parameter. This rearranged thermal conduction equation is shown
354 in Eq. 2

$$355 \quad k_{eff} = \frac{L}{T_2 - T_1} \cdot q'' \quad (2)$$

356 Where k_{eff} is the effective thermal conductivity, T_2 and T_1 are two independent
357 temperature values located at different locations along the chosen axis, L is the distance
358 between T_2 and T_1 along the same axis, and q'' is the heat flux magnitude at the
359 boundary. The temperature distributions produced by the FEM solver provide
360 temperature data corresponding to every node on every element within the finite
361 element model. To apply Eq. 2 across the full particle set and obtain an effective thermal
362 conductivity value for the given set, the output temperature information must be
363 reduced. The temperature distributions were first filtered to only include the external
364 faces corresponding to the minimum and maximum values of the x coordinates. The
365 temperature datasets were again filtered to only include temperature data from particle
366 nodes. This filtration only included particle faces corresponding to non-insulative
367 boundary conditions and allowed for a more accurate temperature difference calculation
368 across the set of particles. Finally, the filtered temperature data was averaged at both the
369 maximum and minimum x-coordinate locations to obtain a single representative

370 temperature value for each location. These average temperatures correspond to T_2 and
 371 T_1 from Eq. 2.

372 Once the output data was simplified to averaged temperature values, the effective
 373 thermal conductivity of the particle group could be determined. Eq. 2 provides a first-pass
 374 estimate for this value, but it is unable to account for non-uniform surface areas in the
 375 primary direction of heat flow, and thus requires modification. The PFM data input is
 376 inherently stochastic, meaning the nanoparticle geometries present in each particle set
 377 are different. Therefore, the surface areas that are exposed to the constant surface
 378 temperature and the constant heat flux boundary conditions can vary considerably
 379 between beds and between timesteps for a given bed. Additionally, the cross-sectional
 380 area perpendicular to the axis of heat flow changes with location in a unique way for each
 381 bed. A correction factor is added to Eq. 2 to account for these sources of variation and
 382 provide more comparable values for the effective thermal conductivity of the particle set.
 383 The modified formulation is shown in Eq. 3.

$$384 \quad k_{eff} = \left(\frac{A_s}{V_f}\right) \cdot \frac{L}{T_2 - T_1} \cdot q'' \quad (3)$$

385 V_f represents the volume fraction of the PFM bounding box taken up by the nanoparticle
 386 models. A_s represents the surface area corresponding to the constant heat flux boundary
 387 condition. T_2 and T_1 correspond to the average temperatures on the filtered external
 388 particle faces, q'' represents the applied heat flux of $10^4 \frac{MW}{m^2K}$ and L represents the
 389 distance between T_2 and T_1 . The fraction shown in Eq. 3 corrects for differences between

390 the surface area where the heat flux and temperature boundary conditions were applied
391 and the average surface area along the axis of heat flow through the particle set. The full
392 calculation was performed on 10 beds for 35 sampled timesteps each. In addition to the
393 thermal conductivity calculation, the density of each nanoparticle packing was calculated
394 using a Python script. This script samples each bed and calculates the ratio of particle
395 volume to the volume of a bounding box. Given the small number of nanoparticles, the
396 bounding box used to determine the total volume was chosen to be a subset of the full
397 PFM bounding box. This reduces the impact of boundary effects on the densification
398 results by focusing on the interior particles that better represent the majority of particles
399 in a much larger bed. The results of the simulations for the 10 randomly generated particle
400 beds were aggregated into a single dataset, shown in Fig. 3.

401 Fig. 3 includes the output data from the thermal simulations and density
402 calculations along with a linear best fit line and prediction bounds. All simulations were
403 run for a fixed number of timesteps, although each bed reached a different density value
404 by the end of the PFM simulation. Many of these density values were substantially larger
405 than the density values achievable during laser sintering (this does not include the
406 annealing process that occurs post-sintering). Therefore, thermal conductivity data points
407 were excluded if their density values exceeded $5000 \frac{kg}{m^3}$, as this is a reasonable upper
408 bound for achievable densification using the μ -SLS system without post-process
409 annealing. The 95% prediction interval provides a confidence band for future predictions
410 using the linear fit shown in Fig. 3. The large range for prediction results from the

411 considerable uncertainty present for single micron particle beds. In smaller particle
412 systems, boundary effects have considerably more impact on the simulation results. To
413 reduce this uncertainty, a subsection of a larger particle bed can be used at the cost of a
414 significant increase in computational expense. The prediction interval in Fig. 3 will be used
415 to quantify the uncertainty in downstream sintering models that incorporate the results
416 from this work.

417 Due to the random nature of the particle bed generation process, beds have
418 different initial densities. To account for this, the results shown in Fig. 3 are plotted as a
419 function of densification percentage in Fig. 4. Densification percentage refers to the
420 percent increase in density from the density value calculated before the onset of
421 sintering.

422 It is noted that these results describe early necking and initial sintering, but do not
423 include the initial thermal conductivity of the nanoparticle packing before sintering
424 occurs. The values for the initial packing condition were recorded separately. This allows
425 for future simulations to have access to a thermal conductivity value for unsintered
426 copper nanoparticles, in addition to a range of thermal conductivity values for copper
427 nanoparticles as they sinter. The difference in average effective conductivities and
428 densities just before and just after the onset of sintering, along with the associated
429 uncertainties, are $9.42 \frac{W}{m \cdot K}$ (798.35% change from initial thermal conductivity) and 1.28
430 $\frac{kg}{m^3}$ (.035% change from initial density) respectively. Despite a small average increase in
431 the density during initial sintering, the thermal conductivity increases nearly by a factor

432 of 10. This is the result of the early neck formation that occurs when adjacent
433 nanoparticles surpass the sintering threshold. During this initial necking phase, the
434 contact regions between nanoparticles grow considerably, opening larger paths for heat
435 to conduct between the particles. At the onset of this process, the formation of these
436 heat pathways results in a very small change in the overall geometry, and therefore the
437 density, of the packing.

438 The thermal conductivity results presented in this paper were compared with
439 literature results for silver nanoparticles during densification. Fig. 5 shows three separate
440 estimations for the effective thermal conductivity of silver nanoparticles [21] in addition
441 to the data obtained in this work.

442 The results developed in this work differ considerably from those derived from
443 literature. This is to be expected, since the literature results focus more on densification
444 values close to the bulk material value and lack a comprehensive overview of the early
445 necking process that occurs in the μ -SLS system. The laser sintering that occurs during the
446 μ -SLS process is heavily impacted by the initial necking phase, so it is critical that the rapid
447 increase in thermal conductivity during this phase is accurately captured. A summary of
448 the complete FEA process is shown in Fig. 6.

449 **FUTURE WORK**

450 The results developed in this work describe the relationship between copper
451 nanoparticle densification and the corresponding increase in the thermal conductivity of
452 a nanoparticle group. This relationship has been integrated into a preliminary part-scale,

453 transient finite element model capable of predicting the thermal evolution of a powder
454 bed during sintering. Each copper element of the part-scale model has its thermal
455 conductivity updated at a series of timesteps based on the temperature history of the
456 element. Moving forward, this part-scale model will be validated against experimental
457 results using a combination of IR camera images, profilometer profiles, and
458 experimentally measured electrical properties. Additionally, this multi-scale modeling
459 effort will be used to input laser parameters and predict the resulting sintered part
460 shapes. This predictive capability will allow for model-based control of laser parameters
461 to achieve optimized part shapes with minimized heat affected zones. Additionally, larger,
462 2 micrometer by 2 micrometer beds can be used to reduce the uncertainty of the resulting
463 linear fit line by reducing the impact of boundary effects on the results. By expanding the
464 size of the bed, the thermal model can take a subsection from the larger bed and run the
465 heat transfer analysis on an interior subsection, avoiding the particles along the edges.

466

467 **CONCLUSION**

468 In this paper, a Finite Element Model (FEM) and a fully scalable data conversion
469 smalls sets of copper nanoparticles. This will facilitate the prediction of heat affected
470 zones (HAZ) during microscale selective laser sintering (μ -SLS). Phase Field Modeling
471 (PFM) data was converted into solid particle CAD models, and an automated steady-state
472 heat transfer simulation was used to calculate temperature profiles and effective thermal
473 conductivities of nanoparticle packings. A steady state, 1D thermal conduction
474 approximation was used alongside an area/volume fraction correction factor to extract

475 thermal conductivity information out of resulting temperature data. The results show a
476 rapid increase in the thermal conductivity during early particle necking, and a reduced
477 rate of change for later timesteps. The results also show that there is significant
478 uncertainty in the thermal conductivity of the beds due to the variances in nanoparticle
479 configurations throughout the bed but that there is a clear trend that as the particle bed
480 starts to sinter together and densify, the thermal conductivity of the bed increases.
481 Overall, the thermal conductivity of the bed almost doubles from initial sintering to the
482 maximum densification that is typically achieved in the μ -SLS process.

483

484 **FUNDING**

485 The authors of this work would like to thank NXP Semiconductors for the generous
486 financial support. This paper contributes to work supported by the National Science
487 Foundation under Grant No. 1728313.

488 **NOMENCLATURE**
489

ρ	variables should appear in first column with the description in second column, m
η	all variables should appear in italics
c_p	two-letter abbreviations should appear in italics
Q'''	three-letter abbreviations should not appear in italics
K	Reynolds number and similar abbreviations do not use italics
ρ	use the "Tab" key to add more rows to this table
k_{eff}	Effective thermal conductivity of the nanoparticle packing
L	Distance between locations corresponding to T_2 and T_1
T_2	Average temperature on the filtered external particle face
T_1	Average temperatures on the opposite side particle faces
q''	Heat flux magnitude at the boundary
A_s	Surface area corresponding to the constant heat flux boundary condition
V_f	Volume fraction of the PFM bounding box taken up by the nanoparticle models

490

491 **REFERENCES**

- 492 [1] Design Guidelines: Laser Sintering (LS), (n.d.). Retrieved June 28, 2017, from
493 <https://www.stratasysdirect.com/resources/laser-sintering/>. [2] B. Sager, D. Rosen,
494 Stereolithography Process Resolution, Georgia Institute of Technology, (n.d.).
- 495 [3] N.K. Roy, D. Behera, O. G. Dibia, Chee S. Foong, M. Cullinan, A novel microscale
496 selective laser sintering (μ - SLS) process for the fabrication of microelectronic parts,
497 *Microsystems and Nanoengineering*, 64 (2019)
- 498 [4] N. K. Roy, C. S. Foong, M. A. Cullinan, Design of a Micro-scale Selective Laser
499 Sintering System, 2016 Annual International Solid Freeform Fabrication Symposium,
500 (2016).
- 501 [5] N. Roy, A. Yuksel, M. Cullinan, Design and Modeling of a Microscale Selective Laser
502 Sintering System, ASME 2016 11th International Manufacturing Science and Engineering
503 Conference, (2016).
- 504 [6] N. Roy, O. Dibia, C. S. Foong, M. Cullinan, Preliminary Results on the Fabrication of
505 Interconnect Structures Using Microscale Selective Laser Sintering, Proceedings of the
506 ASME 2017 International Technical Conference and Exhibition on Packaging and
507 Integration of Electronic and Photonic Microsystems, (2017).
- 508 [7] C. Nelson, K. McAlea, D. Gray, 1995, Improvements in SLS Part Accuracy, Annual
509 International Solid Freeform Fabrication Symposium, (1995) 159-169.
- 510 [8] L. Dong, A. Makradi, S. Ahzi, Y. Remond, 2009, Threedimensional transient finite
511 element analysis of the selective laser sintering process, *Journal of Materials Processing*
512 *Technology*, 209 (2009) 700-706.
- 513 [9] D. Moser, M. Cullinan, J. Murthy, Particle-Scale Melt Modeling of the Selective Laser
514 Melting Process, 2016 Annual International Solid Freeform Fabrication Symposium,
515 (2016) 247-256.
- 516 [10] D. Moser, S. Fish, J. Beaman, J. Murthy, Multi-Layer Computational Modeling of
517 Selective Laser Sintering Processes, ASME 2014 International Mechanical Engineering
518 Congress and Exposition, 2A (2014) V02AT02A008- V02AT02A018.
- 519 [11] O. G Dibia, A. Yuksela , N. K Roy , C. S Foong, M. Cullinan, Nanoparticle Sintering
520 Model, Simulation and Calibration Against Experimental Data, ASME 2018 13th
521 International Manufacturing Science and Engineering Conference, (2018)
- 522 [12] A. Yuksel, E. T. Yu, M. Cullinan, J. Murthy, Investigation of heat transfer modes in
523 plasmonic nanoparticles, *International Journal of Heat and Mass Transfer*, 156, (2020)

- 524 [13] G. K. Batchelor and R. W. O'Brien, Thermal or Electrical Conduction Through a
525 Granular Material, Proceedings of the Royal Society of London. Series A, Mathematical
526 and Physical Sciences, 355 (1977) 313-333
- 527 [14] J. Sun and M. M. Chen, A theoretical analysis of heat transfer due to particle
528 impact, International Journal of Heat and Mass Transfer, 31 (1988) 969- 975
- 529 [15] J. H. Zhou, A. B. Yu, and M. Horio, Finite element modeling of the transient heat 150
530 conduction between colliding particles, Chemical Engineering Journal, 139 (2008) 510-
531 516
- 532 [16] Yoshiyuki Shimizu, Three-dimensional simulation using fixed coarse-grid thermal-
533 fluid scheme and conduction heat transfer scheme in distinct element method, Powder
534 Technology, 165 (2006) 140-152
- 535 [17] J. J. Zhao, Y. Y. Duan, X. D. Wang, B. X Wang, A 3-D numerical heat transfer model
536 for silica aerogels based on the porous secondary nanoparticle aggregate structure,
537 Journal of Non-Crystalline Solids, 358 (2012) 1287-1297
- 538 [18] J. F. Guo, G. H. Tang, A theoretical model for gas- contributed thermal conductivity
539 in nanoporous aerogels, International Journal of Heat and Mass Transfer, 137 (2019) 64-
540 73
- 541 [19] Dongxu Wu, Congliang Huang, Thermal conductivity study of SiC nanoparticle beds
542 for thermal insulation applications, Physica E: Low-dimensional Systems and
543 Nanostructures 118, (2020), 113970
- 544 [20] Zi-Zhen Lin, Cong-Liang Huang, Wen-Kai Zhen, Zun Huang, Enhanced thermal
545 conductivity of metallic nanoparticle packed bed by sintering treatment, Applied
546 Thermal Engineering 119, 425-429 (2017)
- 547 [21] Fei Qin, Yuankun Hu, Yanwei Dai, Tong An, Pei Chen, Evaluation of thermal
548 conductivity for sintered silver considering aging effect with microstructure based
549 model, Microelectronics Reliability 108 (2018)
- 550 [22] R. Ganeriwala, T. I. Zohdi, A coupled discrete element- finite difference model of
551 selective laser sintering. Granular Matter 18, 21 (2016)
- 552 [23] D. Moser, S. Pannala, J. Murthy, Computation of Effective Thermal Conductivity of
553 Powders for Selective Laser Sintering Simulation, Journal of Heat Transfer, 138 (2016)
- 554 [24] Moser, D., Yuksel, A., Cullinan, M., and Murthy, J., Use of detailed particle melt
555 modeling to calculate effective melt properties for powders. Journal of Heat Transfer,
556 140 (2018) 052301.

- 557 [25] Y. Li, D. Gu, Parametric analysis of thermal behavior during selective laser melting
558 additive manufacturing of aluminum powder, *Materials and Design*, 63, (2014) 856-867
- 559 [26] D. Pitassi, E. Savoia, V. Fontanari, A. Molinari, V. Luchin, G. Zappini, M. Benedetti,
560 Finite Element Thermal Analysis of Metal Parts Additively Manufactured via Selective
561 Laser Melting, *Finite Element Method – Simulation, Numerical Analysis and Solution*
562 *Techniques*, (2018)
- 563 [27] Yuksel, A. and Cullinan, M. “Modeling of Nanoparticle Agglomeration and Powder
564 Bed Formation in Microscale Selective Laser Sintering Systems.” *Journal of Additive*
565 *Manufacturing*, 12 (2016) 204-215.
- 566 [28] Dibua, O., Yuksel, A., Roy, N., Foong, C.S., and Cullinan, M., “Nanoparticle Sintering
567 Model, Simulation and Calibration Against Experimental Data.” *Journal of Micro and*
568 *Nanomanufacturing*, 6 (2018) 041004.
- 569 [29] A. Yuksel, E. T. Yu, M. Cullinan, J. Murthy, Thermal transport in nanoparticle
570 packings under laser irradiation, *Journal of Heat Transfer*, 142 (2020)
- 571 [30] H. Zheng, K. Jagannadham, Interface Thermal Conductance Between Metal Films
572 and Copper, *The Minerals, Metals and Materials Society and ASM International* (2014)

573
574
575

Figure Captions List

- Fig. 1 The Full Conversion Process. a). Nanoparticles represented by point clouds; b). Nanoparticles represented by a triangular surface mesh derived from point clouds; c). Nanoparticles represented by solid models derived from triangular surface meshes; d). Nanoparticle solid models resting on a glass substrate; e). Hollowed out air block; f). Full assembly of particles, air, and glass
- Fig. 2 3-Dimensional Finalized Solid Models (Note the 180-degree rotation about the z-axis between images c and d). a). Model with enveloping air block; b). Model without air block; c). Constant surface heat flux boundary condition shown in red; d). Constant surface temperature boundary condition shown in blue
- Fig. 3 Thermal conductivity vs density with linear fit line and 95% prediction bounds
- Fig. 4 Thermal conductivity vs densification percentage with linear fit line and 95% prediction bounds
- Fig. 5 Thermal Conductivity vs Density Comparison: This work vs Qin Et. Al [21]
- Fig. 6 Summary of Finite Element Setup and Sample Results

576

577
578

Table Caption List

Table 1 Capitalize the first word in the caption

579

Fig. 1

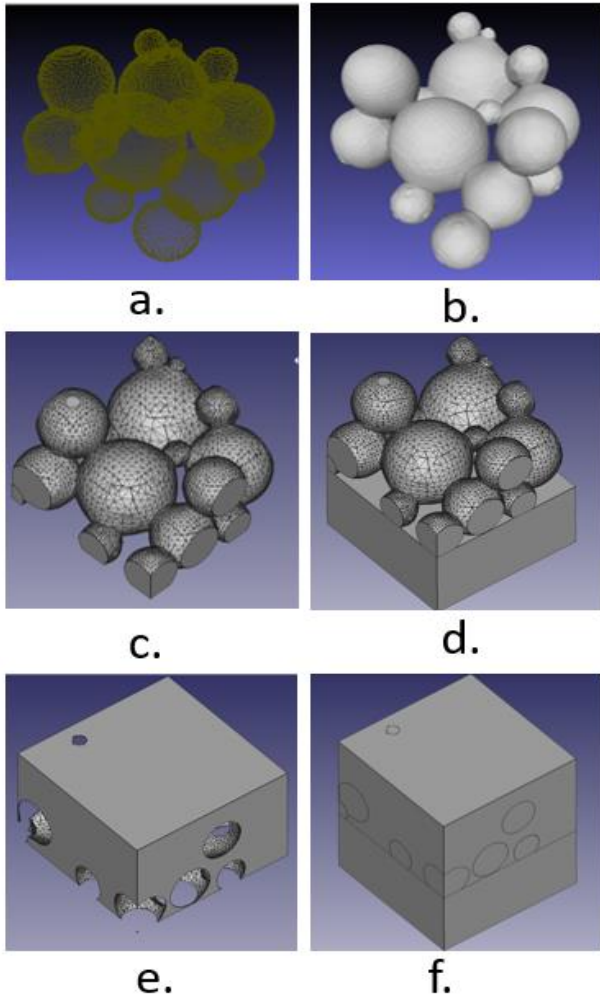
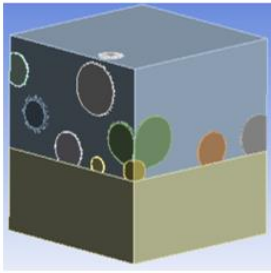
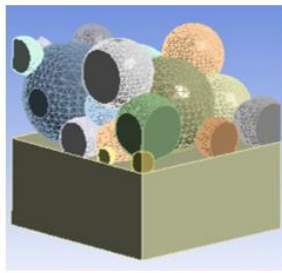


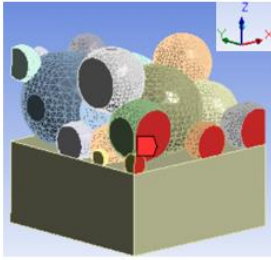
Fig. 2



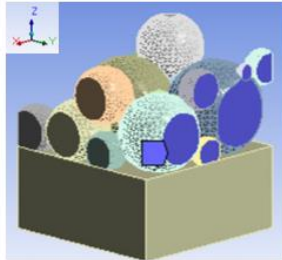
a.



b.



c.



d.

Fig. 3

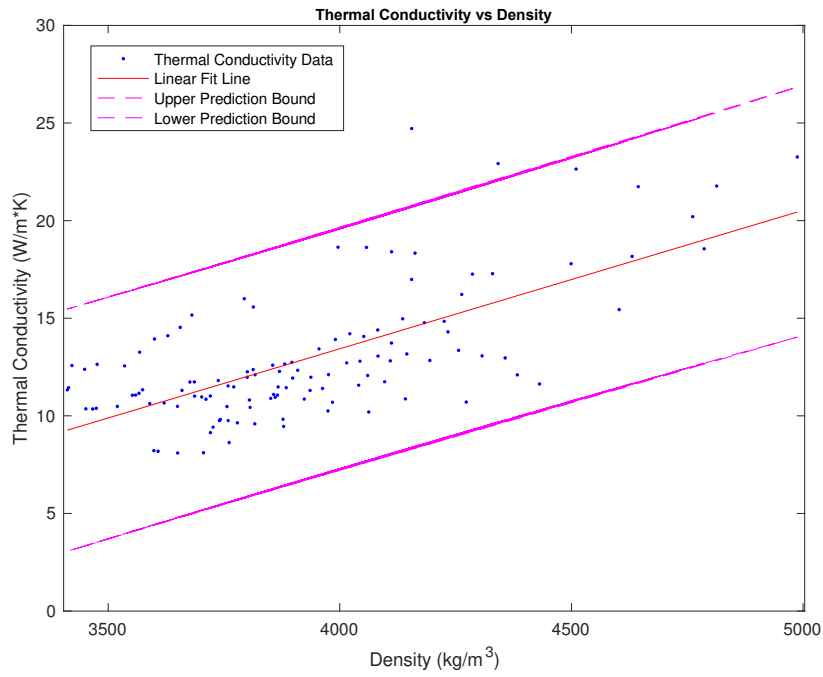


Fig. 4

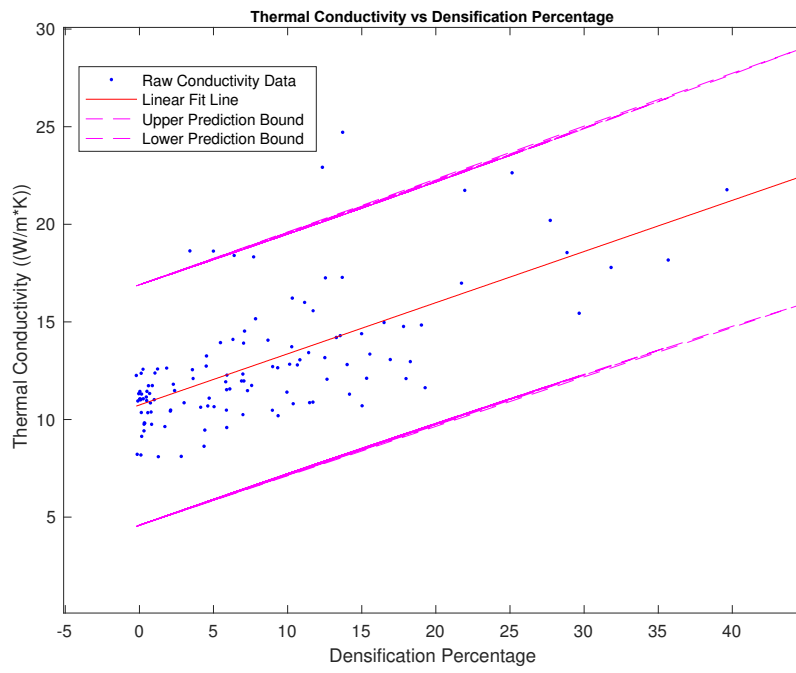


Fig. 5

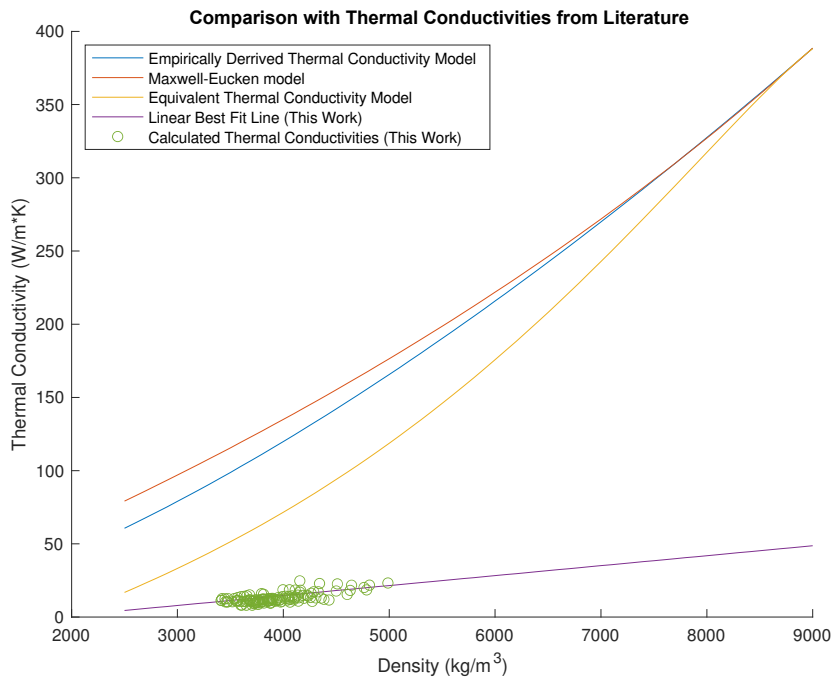


Fig. 6

